INTERNATIONAL JOURNAL FOR NUMERICAL METHODS IN FLUIDS
Int. J. Numer. Meth. Fluids 2006; **50**:1247–1268
Published online 2 December 2005 in Wiley InterScience (www.interscience.wiley.com). DOI: 10.1002/fld.1113

Application of the multidimensional positive definite advection transport algorithm (MPDATA) to environmental modelling on adaptive unstructured grids

Nash'at N. Ahmad[‡], David P. Bacon[*,†], Mary S. Hall[§] and Ananthakrishna Sarma[¶]

Center for Atmospheric Physics, Science Applications International Corporation, 1710 SAIC Drive, McLean, VA 22102, U.S.A.

SUMMARY

Twenty years ago, the multidimensional, positive definite, advection transport algorithm was introduced by Smolarkiewicz. Over the two decades since, it has been applied countless times to numerous problems, however almost always on rectilinear grids. One of the few exceptions is the Operational Multiscale Environment model with Grid Adaptivity (OMEGA), an atmospheric simulation system originally designed to simulate atmospheric dispersion in the planetary boundary layer, but since then used for both mesoscale (from meso-α to meso-γ) dispersion and weather forecasting. One of the unique aspects of OMEGA is the triangular unstructured grid geometry which leads in a natural way to the creation of a global grid with continuously variable resolution from roughly 100 km over the oceans to less than 10 km over regions of interest. Another unique aspect is the concept of dynamically adapting grid resolution—sometimes also called solution-adaptive grid resolution. A central element of the modelling system, however, is its advection solver—MPDATA. This paper presents the implementation of MPDATA on an unstructured grid and demonstrates its accuracy and efficiency using analytic and idealized test cases. Copyright © 2005 John Wiley & Sons, Ltd.

KEY WORDS: MPDATA; numerical methods; unstructured grids; atmospheric simulation; geophysical fluid dynamics

1. INTRODUCTION

In the early days of computing, geophysical fluid dynamics (GFD), predominately numerical weather prediction (NWP), was a dominant factor in the design of computer architecture

*Correspondence to: David P. Bacon, Center for Atmospheric Physics, Science Applications International Corporation, 1710 SAIC Drive, McLean, VA 22102, U.S.A.
†E-mail: david.p.bacon@saic.com
‡E-mail: ahmadn@saic.com
§E-mail: mary.s.shall@saic.com
¶E-mail: sarmaa@saic.com

Contract/grant sponsor: Defense Threat Reduction Agency

Received 25 March 2005
Revised 13 September 2005
Accepted 14 September 2005

and algorithms. This early work focussed initially on solving a finite difference equation on a uniform rectilinear computational grid and later on spectral methods. After the initial work of Charney [1], Charney *et al.* [2], and Arakawa [3], however, the focus shifted from the basic algorithms for the numerical solution of the fundamental differential equations to improvements in the model physics. Further work on fundamental numerical algorithms shifted to other disciplines—predominately the then emerging aerospace community.

In spite of this shift of focus, some researchers continued fundamental work into advection solvers for atmospheric applications. In 1984, Smolarkiewicz introduced the multidimensional positive definite advection transport algorithm (MPDATA) [4]. Since that time, MPDATA has been implemented in numerous atmospheric and other models (e.g. [5–7]), though always based upon a structured rectilinear mesh.

At the same time meteorology was benefiting from this research and technology boom, computational fluid dynamics (CFD) researchers were creating new innovative numerical techniques designed to model fluid flows around complex geometries. In the 1970s and early 1980s the models developed for aerospace engineering and plasma physics were surprisingly similar to their counterparts in the atmospheric sciences. The grids were composed of regular, rectangular cells extending from no-slip or free-slip surfaces. As more computational power became available and atmospheric modellers were implementing more physics into their models, CFD practitioners were busy refining complex gridding techniques around irregular surfaces. One of the methodologies developed was the use of unstructured triangular grids [8, 9].

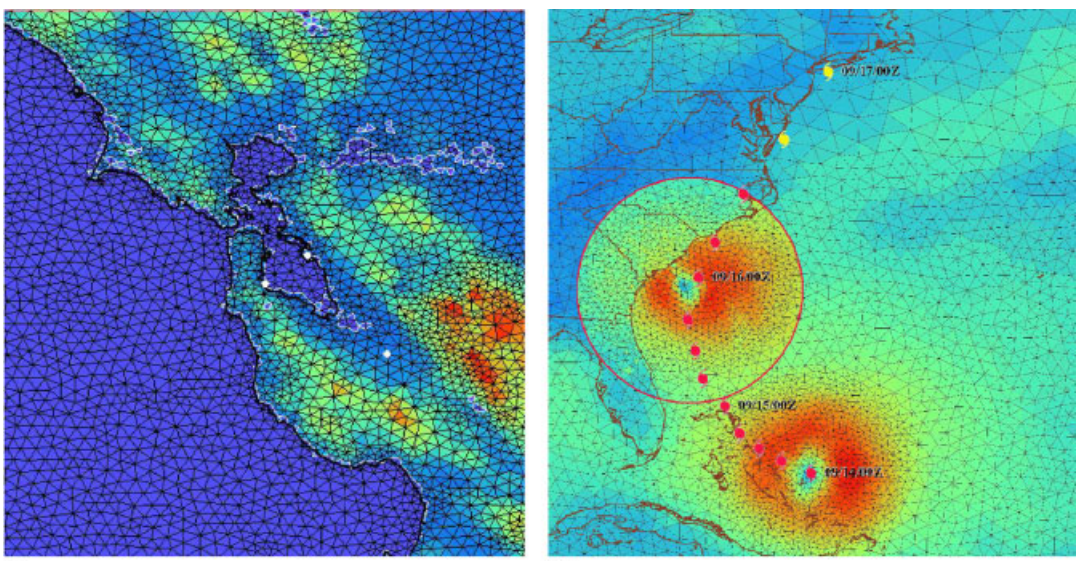

(a) (b)

Figure 1. (a) Static adaptation creates a grid that captures the complex terrain and land/water boundaries; (b) dynamic adaptation puts high resolution only where required leading to computational efficiency. The left panel shows a grid created for the San Francisco Bay area; the right panel shows the Hurricane Floyd (1999) grid and wind speed (shading) at initialization and (inset) the high resolution portion 48 h into the forecast. (The observed storm track is shown at 6 h intervals by the symbols.)

Starting in 1991, this paradigm of unstructured adaptive grids was applied to atmospheric simulations. This paradigm has the advantage of tremendous flexibility in providing high resolution where required by either static physical properties (terrain elevation, coastlines, land use) or the changing dynamical situation (cf. Figure 1). The effort resulted in the Operational Multiscale Environment model with Grid Adaptivity (OMEGA) [10]. The OMEGA model with the embedded atmospheric dispersion model (ADM) is an atmospheric simulation system originally designed for real-time airborne hazard prediction. Because this problem involves extensive interaction between the atmosphere and the surface, the ability to accurately model the terrain features is of paramount importance. OMEGA has demonstrated its ability to accurately predict the transport and diffusion of hazardous releases [11] as well as to accurately forecast the track of hurricanes [12]. Originally designed for regional simulations, the model has since been extended to support the ultimate multiscale modelling challenge—global to local scale atmospheric simulation.

While the gridding scheme utilized in OMEGA was new to atmospheric simulation, the base advection scheme was not. The MPDATA algorithm was adapted to the unstructured mesh. While this was a unique application of MPDATA, it was a natural extension of the original formulation and the details of that adaptation and a demonstration of the results is the topic of this paper.

2. ADAPTIVE UNSTRUCTURED GRIDS

The basis for all computational methods is the assumption that a function $f(x)$ is known at a set of discrete points x_i. The function is then expanded in a Taylor series. While a uniform grid analysis improves the solution by increasing the number of terms of the Taylor series that are retained, an adaptive grid analysis utilizes knowledge of the terms themselves to achieve the same result. A demonstration of this can be seen for the Gaussian function ($f(x) = \mathrm{A}e^{-x^2}$) on the interval from 0 to 10 (Figure 2). A 21-point uniform (grid spacing 0.5) grid and an 11-point nonuniform grid of this function can both have an integral accuracy of 0.5%. Where the slope is constant, however, the adaptive grid represents the function by only a few points. The real benefit of adaptive grids arises when the breadth of scales of the physical system is large. In the case shown in Figure 2, the range of scales was 10 (the domain) to 1 (sigma); in the atmosphere, the range of scales can be far greater.

Unstructured triangular grids are the logical extension of the adaptive grid discussed above into two dimensions. The OMEGA grid generator creates an atmospheric grid by tessellating the surface of the Earth using triangular tiles (cf. Figure 1) and then constructing radii through each of the surface vertices. A set of surfaces is then constructed that are terrain following near the surface and spherical at high altitude. While completely unstructured three-dimensional (tetrahedral) meshes have been used for other purposes [13, 14], the benefit of having a structured vertical dimension in an atmospheric grid is a significant reduction in the computational requirements of the model. Specifically, the structured vertical grid enables the use of a tri-diagonal solver to perform implicit solution of both vertical advection and vertical diffusion. Since in many larger scale applications the vertical grid spacing is one or more orders of magnitude smaller than the horizontal grid spacing, the ability to perform vertical operations implicitly relaxes the limitation on the time-step.

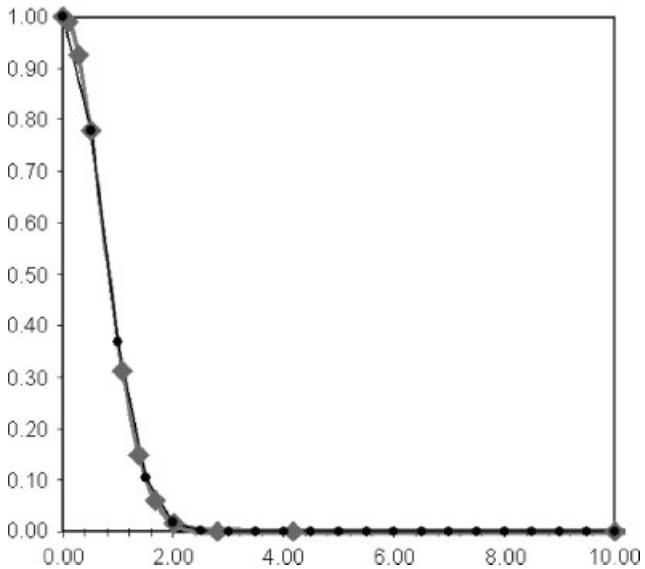

Figure 2. Two representations of a Gaussian. The grey curve represents a 501-point baseline representation, the black curve with dots shows a 21-point representation using a uniformly spaced (grid spacing 0.5) grid, and the diamonds show an 11-point adaptive grid representation.

The flexibility of unstructured grids facilitates the meshing of arbitrary surfaces and volumes in three dimensions. In particular, unstructured grid cells in the horizontal dimension can increase local resolution to better capture topography or the important physical features of atmospheric circulation flows and cloud dynamics. As mentioned in the introduction, the first application of adaptive, unstructured grids to atmospheric simulation is the OMEGA modelling system. A complete description of this system can be found in Bacon *et al.* [10]. Boybeyi *et al.* [11] presents details of the OMEGA ADM and the results of an extensive model evaluation against data from the European Tracer Experiment (ETEX) [15, 16]. Gopalakrishnan *et al.* [12] presents the application of OMEGA, including dynamic adaptation, to hurricane track forecasting and a comparison against observations for 20 forecasts covering 8 storms.

In addition to OMEGA, Varvayanni *et al.* [17] have used unstructured prisms in a diagnostic ADM, which reads in a flow field and interpolates it over the mesh to predict the trajectories of tracers. In their case, they take advantage of the ability of unstructured grids to resolve the underlying terrain in a more realistic and efficient manner. Ghorai *et al.* [18] have used tetrahedral meshes to provide solution-adaptation in both horizontal and vertical, also for atmospheric dispersion calculations. Behrens *et al.* [19] have implemented a semi-Lagrangian advection scheme on unstructured adaptive grids for weather forecasting. These applications have shown the various inherent strengths of unstructured grids such as better representation of topography, computational efficiency (via static or dynamic grid adaptation), and the flexibility of the grid to resolve multiple scales.

3. GRID GENERATION

Since the accurate solution of any complex computational problem depends on adequate spatial discretization of the computational domain, the accurate representation of multiscale events in numerical models has long been a principal issue in CFD. For example, one typically desires to capture not only the development and evolution of small-scale features but also their interaction with and influence upon the larger-scale flow. This is a particularly important requirement in atmospheric models, because numerous events such as fronts, clouds, and plumes are not only relatively localized with respect to their environment, but are also forced on scales larger than their own. Because practical limitations in computer size and speed prohibit the use of uniformly high spatial resolution appropriate for the smallest scales of interest, numerous techniques have been developed to deal with multiscale flows.

Grid nesting techniques involve the sequential placement of multiple finer scale meshes in desired regions of the domain so as to provide increased spatial resolution locally. The decision to spawn one or more sub-meshes is typically subjective and manually directed. Some formulations allow the sub-meshes to move with particular features in the flow, such as hurricanes [20]. A principal limitation of grid nesting technique, however, is that one must know *a priori* and for the duration of the calculation the regions of the domain that will require high spatial resolution. In other words, the trajectory of the moving grid has to be pre-defined and therefore cannot be used for prediction. Another principal limitation of grid nesting technique is the interaction among multiple nested meshes, particularly the tendency for propagating dispersive waves to discontinuously change their speeds upon passing from one mesh to the next and to reflect off the boundaries of each nest due to an impedance mismatch across the mesh boundaries [21].

One advantage of unstructured grids is the ease with which dynamic grid adaptation can be implemented. There is no longer a need for involved user-expertise/interaction for creating topologies of complicated terrain features; the whole procedure can be fully automated, a feature that is not only highly desirable, but is required in operational settings. Also, since the unstructured grid is a single mesh with a smooth and continuous transition from coarse to fine regions within the whole domain, the model is naturally two-way scale interactive without the interpolation error caused by the transfer of information from one nest to another. This also eliminates the wave reflection problem common in nested grid models.

The OMEGA model is currently the only operational atmospheric flow model based on the unstructured grid technique. It can adapt its grid both statically and dynamically to different criteria. *Static* adaptation creates a numerical grid resolving fixed features (e.g. land–water boundaries, terrain gradients, and/or any other feature that the user includes in the adaptation scheme) with a resolution that smoothly varies from the maximum to the minimum specified (Figure 1(a)). In addition, OMEGA grids can be further refined in one or more specific geographical areas that can be specified at the time of grid creation. *Dynamic* adaptation (Figure 1(b)) adds the periodic re-adaptation of the grid to regions that require high resolution during the course of a simulation (e.g. frontal zones, hurricane circulation, pollutant plumes).

3.1. Static grid adaptation

The total number of grid points necessary to perform a successful numerical computation that recovers the correct physics can be greatly reduced in an unstructured grid. By this

we mean that the recovery of the model physics at the smallest length scale resolved does not require the complete domain to have the same resolution. The resources of the numerical and computational machinery are focussed on the regions of importance. This is especially significant for three-dimensional hydrodynamic problems, where our experience has shown the resulting economy can make the difference between tractability and intractability (cf. [8]).

In OMEGA, the adaptation of the unstructured grid takes place through a variety of grid operations including vertex addition, vertex deletion, vertex reconnection, and edge bifurcation (cf. [10]). The OMEGA grid in the 'static' adaptation case is adapted *a priori* to resolve static features such as terrain gradients, land–water boundaries, and/or any other feature that the user includes in the adaptation scheme. The grid can also be refined in one or more specified geographical areas, such as theaters of operation, by the specification of rectangular regions in which higher resolutions are specified. Within each region, grid generation is governed by user-specified minimum and maximum resolutions. The user can alternatively specify a location in the domain and a radius of influence around it; the grid generator will then refine the grid within the region of influence. The result of the use of high-resolution regions and/or circular region refinement is not a nested grid, but a single grid with variable resolution.

An important feature of the unstructured grid is the ability to simulate mountains and coastal features without the 'stair-step' geometry required by nested grid models (cf. [21]). Triangular grids can naturally follow the coastline better, leading to improved land–water circulations, and can better capture the geometry of mountainous regions. This is especially important for near-surface simulations such as those affecting airport terminal operations (cf. Figure 1(a)).

3.2. Dynamic grid adaptation

OMEGA also has the ability to adapt its grid during a simulation to different criteria such as frontal activity, convection, hurricanes [12], and/or a pollutant plume [22]. This enables atmospheric features that require additional grid points for adequate simulation to be resolved as they appear. Thus, through the combination of adaptation methods and criteria, the grid can be coarse where the circulation is regular and smooth, but greatly refined where there are sharp gradients, where topographic features are important, or where model physics or dispersion source terms require fine resolution.

3.3. Global grid generation

The generation of global grids [23] was simplified by the addition of two features: (1) the implementation of an initial icosahedral grid; and (2) a quadrature routine that divides a single triangle into four new triangles. Both of these features are illustrated in Figure 3(a). Given an initial icosahedral grid, the iterative employment of a quadrature six (6) times results in a near-spherical grid with relatively uniform resolution of 125 km (Figure 3(b)). At this point, the usual OMEGA grid generation adaptation to the underlying terrain is enabled resulting in a final grid with continuously variable resolution such as that shown in Figure 3(c). The problems due to polar singularities are also effectively eliminated.

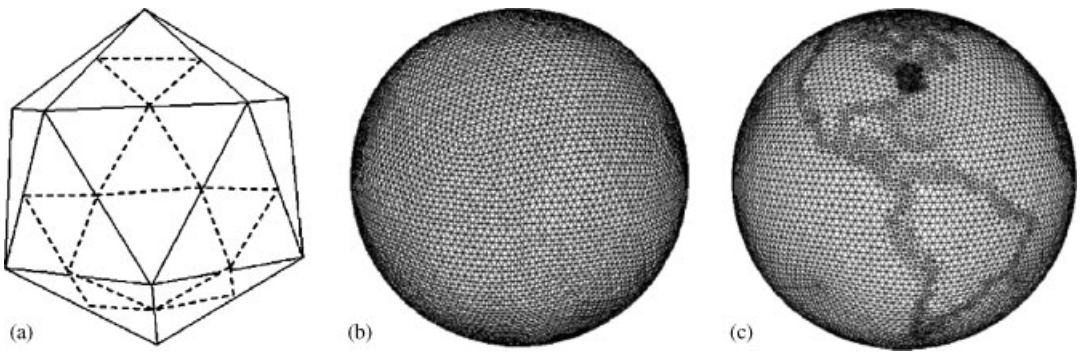

Figure 3. The OMEGA global grids start (a) with an icosohedron, which is then refined using quadrature (dotted lines). After 6 iterative refinements, a roughly uniform mesh (b) is created with resolution ranging from 100 to 150 km. The normal OMEGA adaptation criteria are then applied to create the final mesh (c).

4. MPDATA ON UNSTRUCTURED GRIDS

The hydrodynamic elements of the OMEGA model are based on numerical methods of solution of the Navier–Stokes equations on an unstructured grid in the horizontal direction and a structured grid in the vertical. A standard split-operator methodology is used, calculating advection terms explicitly and diffusion terms implicitly. In the calculation of momentum, the pressure gradient, Coriolis, and buoyancy terms are calculated explicitly along with the advection terms. An implicit vertical filter and an explicit horizontal filter are applied to the vertical momentum. The calculation of the new momentum at each time-step thus involves several steps, which are described below. All implicit operations are performed by tri-diagonal matrix inversion.

MPDATA was originally developed for regular grids by Smolarkiewicz [4], Smolarkiewicz and Clark [24], and Smolarkiewicz and Grabowski [25]. This paper describes the implementation of MPDATA on unstructured triangular prism grids. The resulting scheme is second-order accurate in time and space, conservative, combines the virtues of the MPDATA (e.g. ability to separately ensure monotonicity and positive definiteness) with the flexibility of unstructured grids [13], and can run efficiently on highly parallel computers. The essential methodology is described below along with a demonstration of the method on two-dimensional passive advection test problems.

In discussing unstructured grids, it is necessary to define the nomenclatures. To reiterate, the basic control volume element in our structured–unstructured computational domain is a truncated triangular prism. Each prism is bounded by five faces. For advection across each face, it is convenient to define a local coordinate system with its origin located at the centre of the face. Each face separates the left-hand side (LHS) from the right-hand side (RHS) such that the flow from the LHS cell to the RHS cell is considered positive. For simplicity, the advected variable, hereafter denoted as ψ, is placed at the cell centroid, while the velocity vector is defined on the cell face at the origin of the local coordinate system. Figure 4 shows the basic arrangement of the variables on a two-dimensional grid.

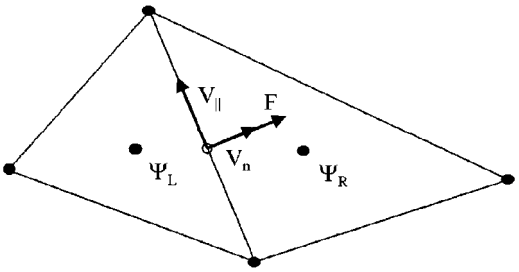

Figure 4. Arrangement of the variables on a two-dimensional unstructured grid. The generic advected variable, ψ, is placed at cell centroids. The subscripts L and R designate their left- and right-hand side cell placements. The velocity is decomposed into normal and parallel components (relative to the common edge). The flux F is co-located with V_n at the face centres, and points in the normal direction.

In its explicit form MPDATA adapts naturally to the above construct. As posed by Smolarkiewicz, the algorithm can be generalized to the following steps:

(1) At each cell face the low-order flux is found in conservative form using the standard first-order-accurate 'upwind' scheme;
(2) The advected variable is integrated using the low-order flux;
(3) At each cell face, the low-order scheme is expanded in a Taylor series and the truncation error in the flux is explicitly identified;
(4) The error term is cast in the form of error velocity, $\mathbf{V}_e$;
(5) The correction velocity, $\mathbf{V}_c$ $(=-\mathbf{V}_e)$, is optionally limited to preserve monotonicity of the advected variable [25];
(6) Replacing $\mathbf{V}$ with $\mathbf{V}_c$, steps (1)–(5) are repeated a chosen number of times $(=N_c)$ to achieve greater accuracy.

Although Smolarkiewicz derived $\mathbf{V}_c$ for a rectangular grid, it can be generalized to a grid with arbitrary control volume shape as long as the bounding faces are flat. Consider the generic advection equation

$$\frac{\partial \Psi}{\partial t} + \vec{\nabla} \cdot (\vec{\mathbf{V}} \Psi) = 0 \tag{1}$$

To compute the change in ψ from time $t = t_0$ to $t_0 + \Delta t$, it is necessary to integrate the flux $\Psi_j \vec{\mathbf{V}}_j$ through each face j during the period Δt:

$$\Delta \Psi_j = \int_{t_0}^{t_0 + \Delta t} \Psi_j \vec{\mathbf{V}}_j \cdot \vec{\mathbf{a}}_j \, \mathrm{d}t \tag{2}$$

Here $\vec{\mathbf{a}}_j = a_j \hat{\mathbf{e}}_n$ is the area vector of face j, where $\hat{\mathbf{e}}_n$ denotes the unit vector normal to the face and pointing from left to right. For this integral, second-order accuracy in space is achieved automatically by placing $\vec{F} = \Psi_j \vec{\mathbf{V}}_j$ at the centre of each face (in practice, Ψ_j at the faces is obtained by interpolation). Similarly, to ensure second-order accuracy in time, $\Psi_j \vec{\mathbf{V}}_j$ should be evaluated at $t = t_0 + \Delta t/2$. Assuming that a leapfrog algorithm is used (i.e. $\vec{\mathbf{V}}_j$ is defined

at $t = t_0 + \Delta t/2$), we need only expand Ψ_j in a Taylor series as

$$\Psi_j = \Psi_j^0 + \frac{\partial \Psi_j}{\partial t}\frac{\Delta t}{2} + O(\Delta t^2) \tag{3}$$

where the superscript 0 denotes an evaluation at $t = t_0$. Substituting (3) for Ψ_j in (1) and performing the time integral, (2) becomes

$$\Delta \Psi_j = \left\{ \Psi_j^0 + \frac{\partial \Psi_j}{\partial t}\frac{\Delta t}{2} \right\} \vec{\mathbf{V}}_j \cdot \vec{\mathbf{a}}_j \Delta t \tag{4}$$

Now substituting (1) for $\partial \Psi / \partial t$ in (4) we have

$$\Delta \Psi_j = \left\{ \Psi_j^0 - [\vec{\mathbf{V}}_j \cdot \vec{\nabla} \Psi_j + (\vec{\nabla} \cdot \vec{\mathbf{V}}_j)\Psi_j]\frac{\Delta t}{2} \right\} \vec{\mathbf{V}}_j \cdot \vec{\mathbf{a}}_j \Delta t \tag{5}$$

If we further let $v_\mathrm{n} = \vec{\mathbf{V}}_j \cdot \hat{\mathbf{e}}_\mathrm{n}$ denote the component of the velocity normal to the face (and thus $\vec{\mathbf{V}}_\mathrm{n} = v_\mathrm{n} \hat{\mathbf{e}}_\mathrm{n}$), then the first-order upwind flux term is given by

$$\Delta \Psi_j^{\mathrm{upwind}} = \tfrac{1}{2}\{(\vec{\mathbf{V}}_\mathrm{n} + \|v_\mathrm{n}\| \hat{\mathbf{e}}_\mathrm{n})\Psi_\mathrm{L} + (\vec{\mathbf{V}}_\mathrm{n} - \|v_\mathrm{n}\| \hat{\mathbf{e}}_\mathrm{n})\Psi_\mathrm{R}\} \cdot \vec{\mathbf{a}}_j \Delta t \tag{6}$$

Now letting $\vec{\delta}_\mathrm{L}$ denote the vector pointing from the cell centroid on the left to the face centroid, and $\vec{\delta}_\mathrm{R}$ the vector pointing from the face centroid to the cell centroid on the right, we can write

$$\Psi_\mathrm{L} = \Psi_j - \vec{\delta}_\mathrm{L} \cdot \vec{\nabla} \Psi_j \tag{7a}$$

and

$$\Psi_\mathrm{R} = \Psi_j + \vec{\delta}_\mathrm{R} \cdot \vec{\nabla} \Psi_j \tag{7b}$$

Similarly, we will let

$$\delta \Psi_\mathrm{L} = \Psi_j - \Psi_\mathrm{L} \tag{8a}$$

and

$$\delta \Psi_\mathrm{R} = \Psi_\mathrm{R} - \Psi_j \tag{8b}$$

Now we can rewrite (4) as

$$\Delta \Psi_j^{\mathrm{upwind}} = \{\vec{\mathbf{V}}_\mathrm{n} \Psi_j^0 - \tfrac{1}{2}\|v_\mathrm{n}\| \hat{\mathbf{e}}_\mathrm{n}(\delta_\mathrm{L}\Psi + \delta_\mathrm{R}\Psi)\} \cdot \vec{\mathbf{a}}_j \Delta t \tag{9}$$

The correction term is the difference between (4) and (9). After some algebraic manipulation, this correction term can be written as

$$\Delta \Psi_\mathrm{c} = \left\{ \|v_\mathrm{n}\| \left(\frac{\Psi_\mathrm{R} - \Psi_\mathrm{L}}{\Psi_\mathrm{R} + \Psi_\mathrm{L}} \right) - v_\mathrm{n} \left[\vec{\mathbf{V}}_j \cdot \frac{\vec{\nabla} \Psi_j}{\bar{\Psi}} + (\vec{\nabla} \cdot \vec{\mathbf{V}}_j) \right] \frac{\Delta t}{2} \right\} \bar{\Psi} a_j \Delta t \tag{10}$$

where $\bar{\Psi} = (\Psi_\mathrm{R} + \Psi_\mathrm{L})/2$.

The magnitude of the correction velocity is now

$$v_c = \|v_n\| \left(\frac{\Psi_R - \Psi_L}{\Psi_R + \Psi_L} \right) - v_n \left[\vec{\mathbf{V}}_j \cdot \frac{\vec{\nabla}\Psi_j}{\bar{\Psi}} + (\vec{\nabla} \cdot \vec{\mathbf{V}}_j) \right] \frac{\Delta t}{2} \tag{11}$$

In actual implementation, the correction term becomes

$$\Delta\Psi_c = \left\{ \|v_n\| \left(\frac{\tilde{\Psi}_R - \tilde{\Psi}_L}{\tilde{\Psi}_R + \tilde{\Psi}_L} \right) - v_n \left[\frac{\vec{\mathbf{V}}_j \cdot \vec{\nabla}\tilde{\Psi}_j}{\bar{\tilde{\Psi}}} + \vec{\nabla} \cdot \vec{\mathbf{V}}_j \right] \frac{\Delta t}{2} \right\} \tilde{\Psi}_{L,R} a_j \Delta t \tag{12}$$

where $\tilde{\Psi}$ is the value of the advected quantity following the first-order upwind advection step.

We limit the number of correction steps to $N_c = 1$, since additional correction steps are not cost effective. The effect of additional correction steps is to bring the solution closer to second-order accuracy, which is very nearly achieved with just one correction step; the additional accuracy attainable is limited.

5. MUSCL-TYPE SCHEME FOR COMPARISON

The description of a monotone upstream-centred scheme for conservation laws (MUSCL) scheme used to compare against MPDATA is given in this section. Higher-order accuracy in space for the Godunov method [26] can be achieved by constructing piecewise linear data from cell averages [27]:

$$\Psi_L = \Psi_{il} + (x_{face} - x_{il}) L_{face} \frac{\partial \Psi_{il}}{\partial x} + (y_{face} - y_{il}) L_{face} \frac{\partial \Psi_{il}}{\partial y} \tag{13}$$

$$\Psi_R = \Psi_{ir} + (x_{face} - x_{ir}) L_{face} \frac{\partial \Psi_{ir}}{\partial x} + (y_{face} - y_{ir}) L_{face} \frac{\partial \Psi_{ir}}{\partial y} \tag{14}$$

where Ψ_L is the extrapolated value of the conserved quantity Ψ on the left-hand side of the face of the control volume, the subscript 'il' is used for the cell centre quantities in the cell on the left of the face, e.g. Ψ_{il} is the cell-averaged value of the conserved quantity Ψ and (x_{il}, y_{il}) are the cell centre coordinates of the cell on the left. Similarly, Ψ_R is the extrapolated value of the conserved quantity Ψ on the right-hand side of the face, the subscript 'ir' is used for the cell centre quantities in the cell on the right of the face, e.g. Ψ_{ir} is the cell-averaged value of the conserved quantity Ψ and (x_{ir}, y_{ir}) are the cell centre coordinates of the cell on the right. The point of intersection between the face and the line connecting the centres of the two cells on either side of the face is denoted by (x_{face}, y_{face}). L_{face} is the limiter on the gradient to ensure a monotonic solution. For higher spatial accuracy, these extrapolated values are used in the flux calculations instead of cell-centred averages.

The piecewise linear reconstruction of data is bounded by enforcing the following condition [28]:

$$\Psi_j^{min} \leqslant \Psi(x, y)_j \leqslant \Psi_j^{max} \tag{15}$$

where

$$\Psi_j^{min} = \min_{i \in N_j} (\Psi_j, \Psi_i) \tag{16}$$

and

$$\Psi_j^{\max} = \max_{i \in N_j} (\Psi_j, \Psi_i) \tag{17}$$

where N_j are the neighbours of the cell j. The limiter L_{face} can now be determined by

$$L_{\text{face}} = \begin{cases} \min\left(1, \dfrac{\Psi_j^{\max} - \Psi_0}{\Psi^{\text{face}} - \Psi_0}\right) & \text{if } \Psi^{\text{face}} - \Psi_0 > 0 \\ \min\left(1, \dfrac{\Psi_j^{\min} - \Psi_0}{\Psi^{\text{face}} - \Psi_0}\right) & \text{if } \Psi^{\text{face}} - \Psi_0 < 0 \\ 1 & \text{if } \Psi^{\text{face}} - \Psi_0 = 0 \end{cases} \tag{18}$$

where Ψ_0 is the cell-averaged value and Ψ^{face} is the extrapolated value on the face of the cell. Three values of L_{face} are obtained for each cell (one for each face) from (18) and the minimum of the three is used to limit the gradient at the cell centre. The gradients are calculated using the Green–Gauss gradient reconstruction.

6. IDEALIZED ADVECTION TESTS

To test the implementation of MPDATA on an unstructured grid, several analytic and idealized test problems were used. The first was a convergence study in which a tracer field (Gaussian function) is rotated in two-dimensions on meshes of varying resolutions. The second was the deformational flow first proposed by Smolarkiewicz [29]. The third is the Doswell [30] frontogenesis case and the final test problem was a solution-adaptive case study.

In all of these cases, the following statistics are used for comparison purposes. The root-mean-squared (RMS) error is given by

$$E_{\text{rms}} = \sqrt{\frac{1}{\text{ncells}} \sum_{i=1}^{\text{ncells}} (q_i^{\text{exact}} - q_i^{\text{computed}})^2} \tag{19}$$

while the error is defined in terms of the L2-norm [31]:

$$E_{\text{L2}} = \sqrt{\sum_{i=1}^{\text{ncells}} (q_i^{\text{exact}} - q_i^{\text{computed}})^2 A_i} \tag{20}$$

where ncells is the total number of cells in the mesh and A_i is the area of each cell. The phase error is defined as the distance between the location of the exact maximum and the computed maximum [6]:

$$E_{\text{phase}} = \sqrt{(x^{\text{exact}} - x^{\text{computed}})^2 + (y^{\text{exact}} - y^{\text{computed}})^2} \tag{21}$$

where x^{exact} and y^{exact} are the coordinates of the cell in which the tracer maxima lies for the exact solution and x^{computed} and y^{computed} are the coordinates of the cell in which the maxima

lies for the computed solution. The diffusion error was found by subtracting the computed tracer maxima from the exact value of the tracer maxima [6]:

$$E_{\text{diffusion}} = \max(q^{\text{exact}}) - \max(q^{\text{computed}}) \tag{22}$$

6.1. Convergence study

A convergence study was performed to demonstrate the order of accuracy of the scheme. The domain was bounded within $[-50, 150] \times [0, 173.2051]$ and consisted of only equilateral triangles. This ensured a factor of 2 increase in mesh resolution at each successive refinement of the mesh. A smooth Gaussian cone function was initialized, centred at $(x_c, y_c) = (50, 0.67 y_{\max})$:

$$q(x, y) = \exp(-0.005r) \tag{23}$$

$$r = (x - x_c)^2 + (y - y_c)^2 \tag{24}$$

The rotational flow field was defined as

$$\begin{aligned} u(x, y) &= -\omega(y - y_0) \\ v(x, y) &= \omega(x - x_0) \end{aligned} \tag{25}$$

where $u(x, y)$ and $v(x, y)$ are the velocities in the x- and y-direction, respectively, $\omega = 0.1$ is the constant angular velocity and (x_0, y_0) is the centre of the mesh. The simulation was run for 62.8487 s, which is the time taken by the cone to complete one revolution $= 2\pi/\omega$. The tests were run using four (4) schemes: (1) upwind; (2) (MUSCL)-type with slope limiter; (3) (MUSCL)-type with no limiter; and (4) the MPDATA scheme.

Transmissive boundary conditions were defined with the help of ghost cells [32] which are mirrors of the boundary cells. The solution was marched in time using a two-stage explicit Runge–Kutta scheme [33]. A CFL criteria of 0.9 was set for all four schemes. Green–Gauss gradient-reconstruction was used to achieve higher-order spatial accuracy for the MUSCL-type scheme described in [34].

Figure 5 shows the concentration contours after one revolution for the different schemes; the comparison with the exact solution is shown in Figure 6, which shows concentration profiles at $y = 115.47$ for x between 0 and 100. The errors and timings for the different schemes are shown in Figure 7. The mesh resolutions ($\mathrm{d}x$), errors (error in the L2-norm, E_{L2}; RMS error E_{rms}; diffusion error, $E_{\text{diffusion}}$; and the phase error, E_{phase}), timings (time_{cpu}) and the order of accuracy (p_{L2} and p_{rms}) for the MPDATA and MUSCL-type scheme are tabulated in Tables I and II. The calculations were made on an AMD Opteron (2.19 GHz) running SuSE Linux 9.3 with the timing obtained by the simple expedient of using the Linux 'time' command.

Figure 5 shows the improvement in accuracy and shape preservation by implementing one iteration of correction step of the MPDATA scheme in the baseline upwind scheme. For reference, the results are also compared with a MUSCL-type scheme and the MUSCL-type scheme with no limiter. The comparison with the exact solution is shown in Figure 6, which shows concentration profiles at $y = 115.47$ for x between 0 and 100. The MPDATA scheme is slightly more diffusive than the MUSCL-type scheme (the result of MUSCL-type with no limiter is also plotted for reference). The results of the convergence study are shown in Figure 7. The MPDATA scheme shows second-order convergence as the mesh resolution

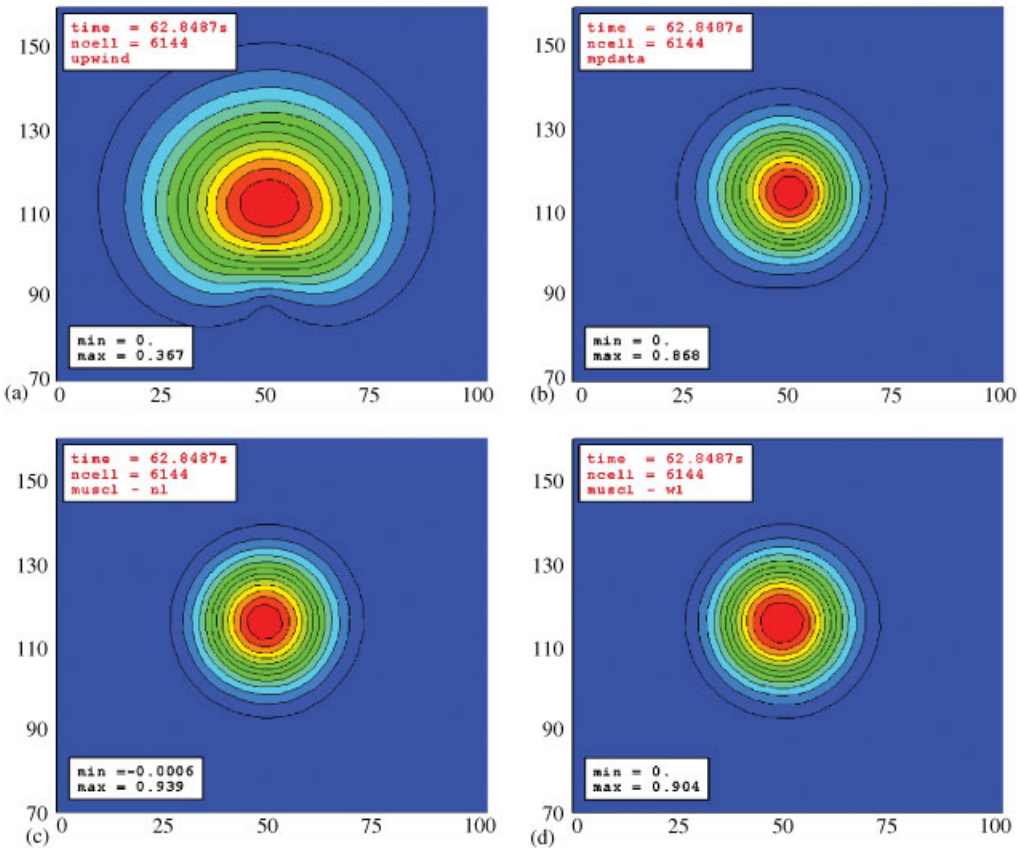

Figure 5. The results of a rotating Gaussian cone test using: (a) an upwind scheme; (b) MPDATA scheme; (c) a MUSCL-type with no limiter; and (d) a MUSCL-type scheme with limiter after one revolution ($t = 62.8487$ s).

approaches zero in the RMS error, the trend is not clear in the L_2-norm. The average order of accuracy in both the L_2 and RMS error is 1.67 for the MPDATA scheme, whereas the average order of accuracy for the MUSCL-type scheme with slope limiter is 1.89 in the L_2 error and 1.87 in the RMS error. The MUSCL-type scheme is less diffusive than the MPDATA scheme. The shape-preservation is better for the MUSCL-type scheme on a coarse resolution mesh shown in Figure 5, but becomes similar for both MPDATA and MUSCL-type solutions on high resolution meshes. The MPDATA scheme, however is approximately 1.3 times faster on the finest mesh. The phase error for the MPDATA scheme is much larger on coarse resolution meshes but improves as the mesh resolution is increased and becomes less than the error in MUSCL-type scheme.

6.2. *Smolarkiewicz's deformational flow test*

The deformational flow problem, first proposed by Smolarkiewicz [29] and later analysed by Staniforth *et al.* [35], is often used for a qualitative evaluation of advection schemes for

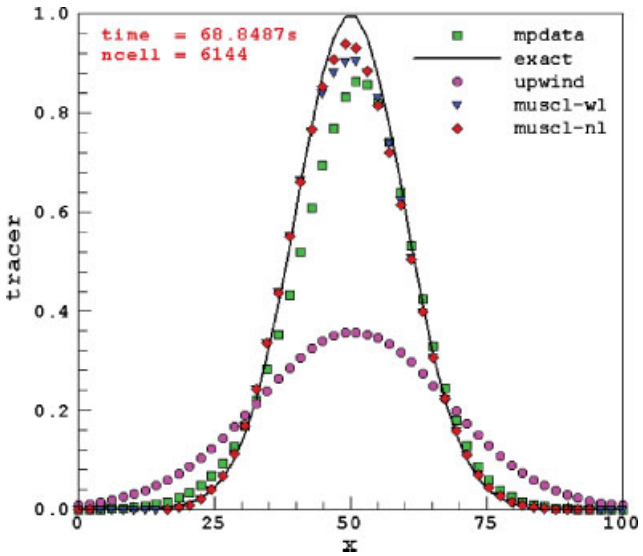

Figure 6. Comparison of the results of upwind, MUSCL-type with limiter, MUSCL-type with no limiter and MPDATA schemes for a rotating Gaussian hill test with the exact solution after one revolution. The profiles shown are at $y = 115.47$ for x varying from 0 to 100 ($t = 68.8487$ s).

atmospheric flow simulations (e.g. [36]). The flow field for the deformation test consists of sets of symmetrical vortices and is given by

$$u(x, y) = Ak \sin(kx) \sin(ky)$$
$$v(x, y) = Ak \cos(kx) \cos(ky) \tag{26}$$

where $u(x, y)$ and $v(x, y)$ are again the velocities in the x- and y-directions, respectively, $k = 4\pi/L$, $A = 8$ and $L = 100$ units. The domain was bounded by $[0, 100] \times [0, 100]$. The unstructured mesh was defined in terms of boundary edges (100 edges on each side). The resulting mesh consisted of 38 510 triangles with the edge lengths ranging from 0.42 to 1.28 m. A tracer cone with a height of 1 unit and radius of 15 units was initialized in the middle of the domain. The mesh, boundary conditions, gradient reconstruction technique, were the same as in the rotating cone test. A four-stage Runge–Kutta explicit scheme was used to march the solution in time. Figure 8 shows the tracer distribution at time $= T/50$ ($T = 2637.6$ s is the final time of integration used in [29]). Figure 9 shows the comparison with Staniforth's analytical solution for tracer values between $x = 25$ and 50, for $y = 50$. The profiles of the computed tracer field are generated by interpolating the data from the cell centres closest to points on the line $(25, 50)$–$(50, 50)$. The Staniforth solution is computed numerically and requires an input of sampling interval. For the comparison shown in Figures 8 and 9, a sampling interval of 0.1 was used. Staniforth *et al.* [35] discussed this test case in detail. They point out that for a mesh resolution of 1 used in [29], the numerical solution is valid only for time $\leqslant T/50$. After time $> T/50$ the features of the tracer field become too small to be effectively captured by a mesh resolution of 1, normally used for this test.

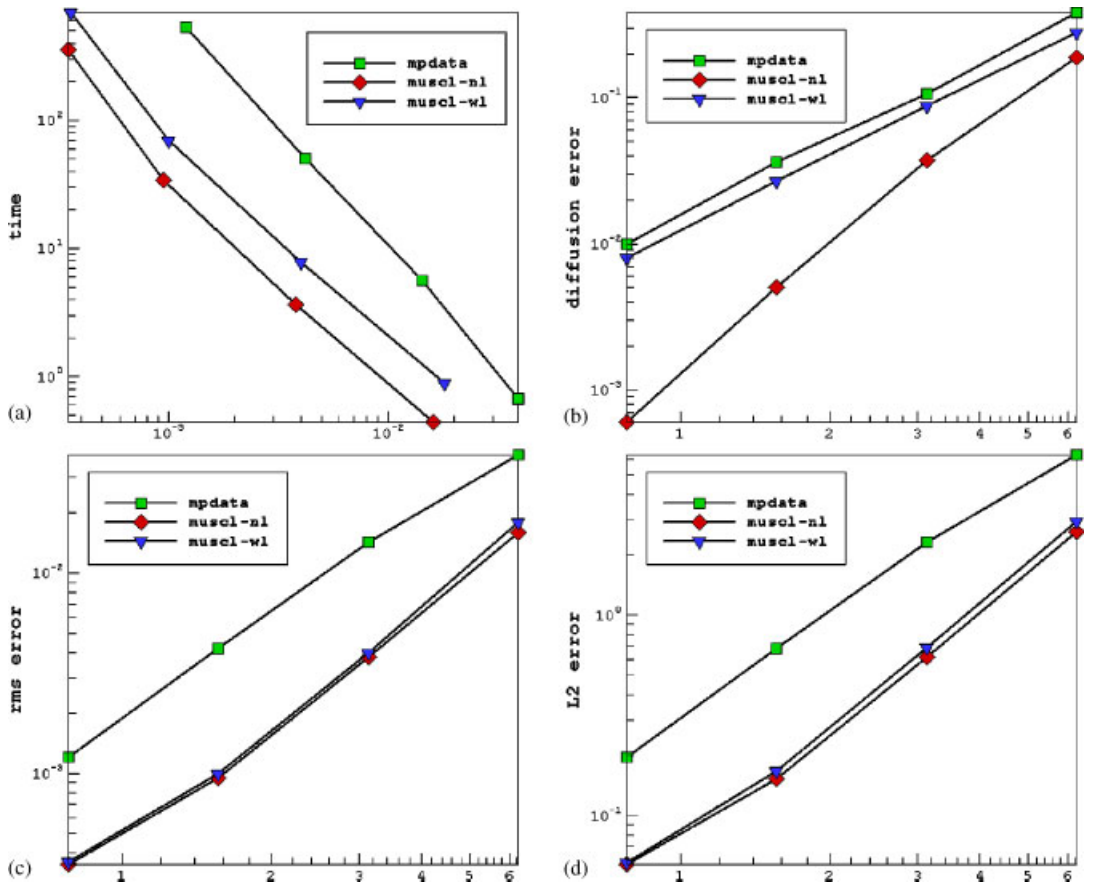

Figure 7. Reduction in error for different schemes with increase in mesh resolution and the associated computational cost.

Table I. MPDATA.

dx	E_{L2}	p_{L2}	E_{rms}	p_{rms}	$E_{diffusion}$	E_{phase}	time$_{cpu}$
6.25000	6.302	—	0.0390	—	0.382	7.216	0.668
3.12500	2.314	1.45	0.0143	1.45	0.106	1.804	5.613
1.56250	0.680	1.92	0.0042	1.77	0.036	0.902	50.38
0.78125	0.196	1.63	0.0012	1.81	0.010	0.000	530.346

6.3. *Doswell's frontogenesis test*

The Doswell frontogenesis problem [30, 37] is an idealized model describing the interaction of a nondivergent vortex with an initially straight frontal zone. The flow field was defined

Table II. MUSCL-type with Barth–Jesperson slope limiter.

dx	E_{L2}	p_{L2}	E_{rms}	p_{rms}	$E_{diffusion}$	E_{phase}	time$_{cpu}$
6.25000	2.932	—	0.0180	—	0.279	3.608	0.891
3.12500	0.692	2.08	0.0041	2.13	0.088	3.125	7.771
1.56250	0.166	2.06	0.0010	2.00	0.027	1.563	70.244
0.78125	0.058	1.52	0.00036	1.47	0.008	1.193	694.5

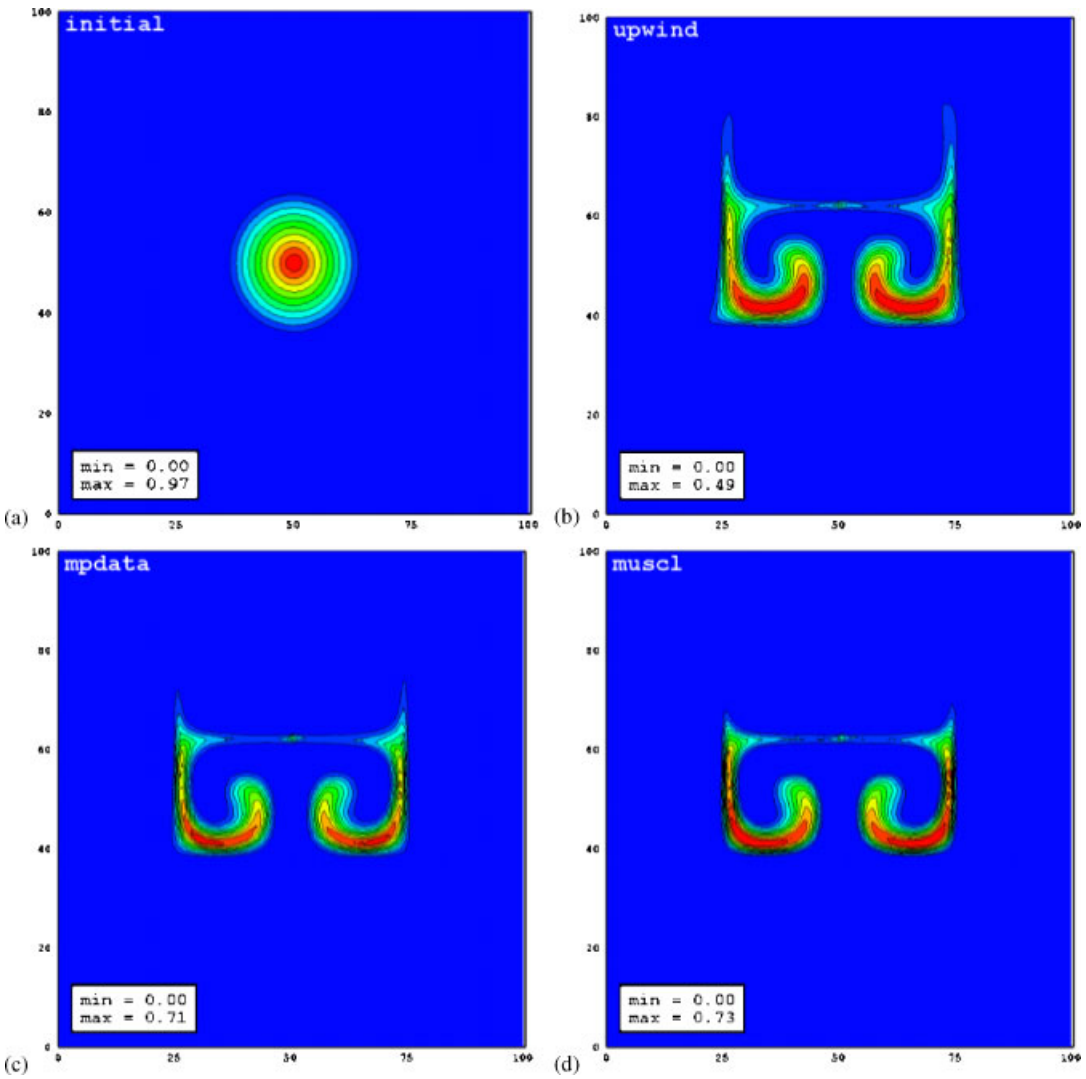

Figure 8. The initial conditions (a), and the results of the Smolarkiewicz deformational flow test using (b) an upwind scheme, (c) MPDATA, and (d) a MUSCL-type scheme with slope limiter at $t = T/50$ (52.752 s) into the simulation (bottom) ($T = 2637.6$ s).

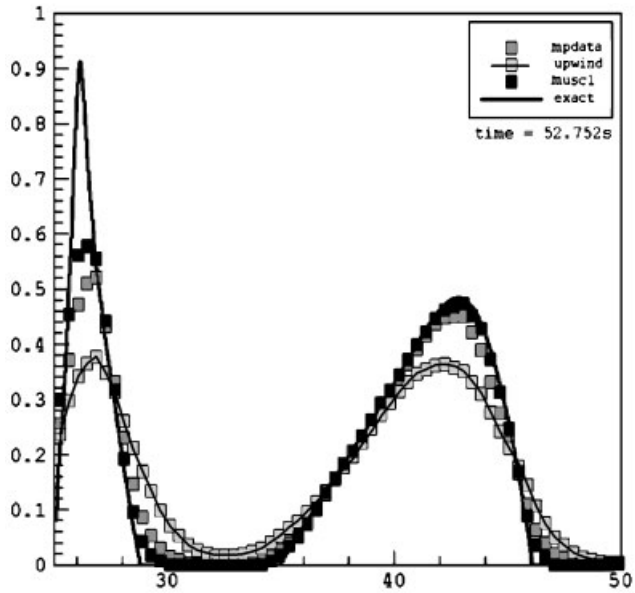

Figure 9. Comparison of the results of upwind, MUSCL-type and MPDATA schemes for a deformational flow test with the exact solution at time $T/50 = 52.752$ s. The values for x between 25 and 50 are shown for $y = 50$. The sampling interval was set to 0.1 for the analytical solution ($T = 2637.6$ s).

as follows:

$$u(x, y) = -\frac{y}{r}\frac{f_t}{f_{\max}} \equiv -yf$$
$$v(x, y) = \frac{x}{r}\frac{f_t}{f_{\max}} \equiv xf \tag{27}$$

where $u(x, y)$ and $v(x, y)$ are the velocities in the x- and y-directions, respectively, r is the distance from any given point to the origin of the coordinate system, $f_{\max} = 0.385$ is the maximum tangential velocity and f_t is given by

$$f_t = \frac{\tanh(r)}{\cosh^2(r)} \tag{28}$$

The triangular domain consisted of equilateral triangles with edge length $= 0.09$. The mesh had a total of 16 384 cells. The boundary conditions and the time-marching scheme were the same as in the rotating cone test. The simulation was run for $t = 4$ s. The evolution of tracer field in time t, is given by the exact solution:

$$q(x, y, t) = -\tanh\left[\frac{y}{\delta}\cos(ft) - \frac{x}{\delta}\sin(ft)\right] \tag{29}$$

where δ is set to 2 for a smooth frontogenesis.

Figure 10 shows the initial conditions and a comparison between the exact and the numerical solutions. The simulation results are in good agreement with the exact solution. For example,

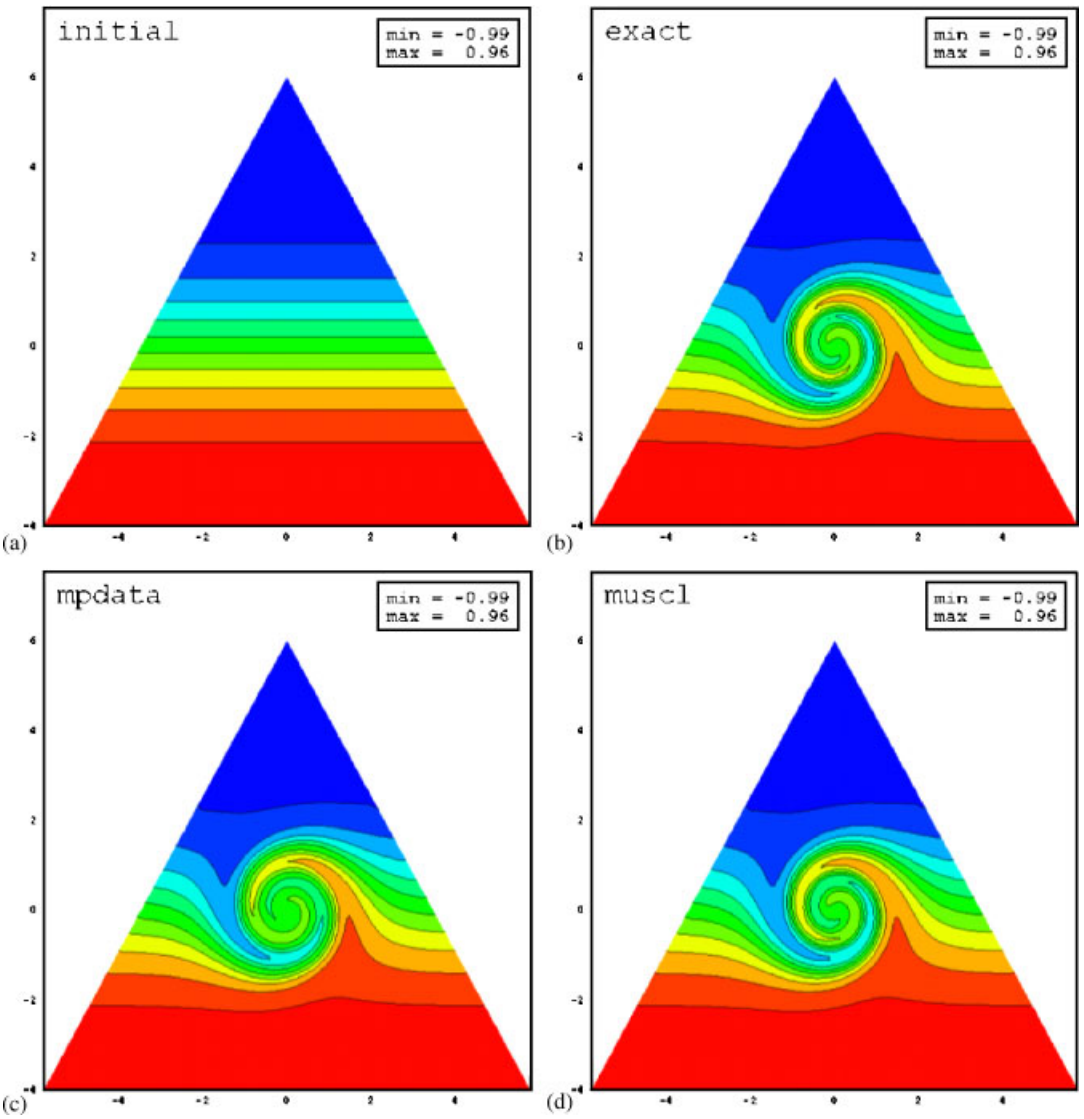

Figure 10. The initial conditions (a), and the exact solution (b) for the Doswell frontogenesis test compared with the solution using (c) MPDATA scheme, and (d) a MUSCL-type scheme with slope limiter at $t = 4$ s.

the Doswell analytical solution predicts the maximum deformation of the frontal zone near the radius of maximum winds and this result is accurately reproduced by the numerical model in both the MPDATA and MUSCL implementations.

6.4. Solution-adaptation

As a final test, the rotating-cone test was used to demonstrate the advantages of the solution-adaptive technique. The domain was bounded within $[0, 100] \times [0, 100]$. The cone was centred

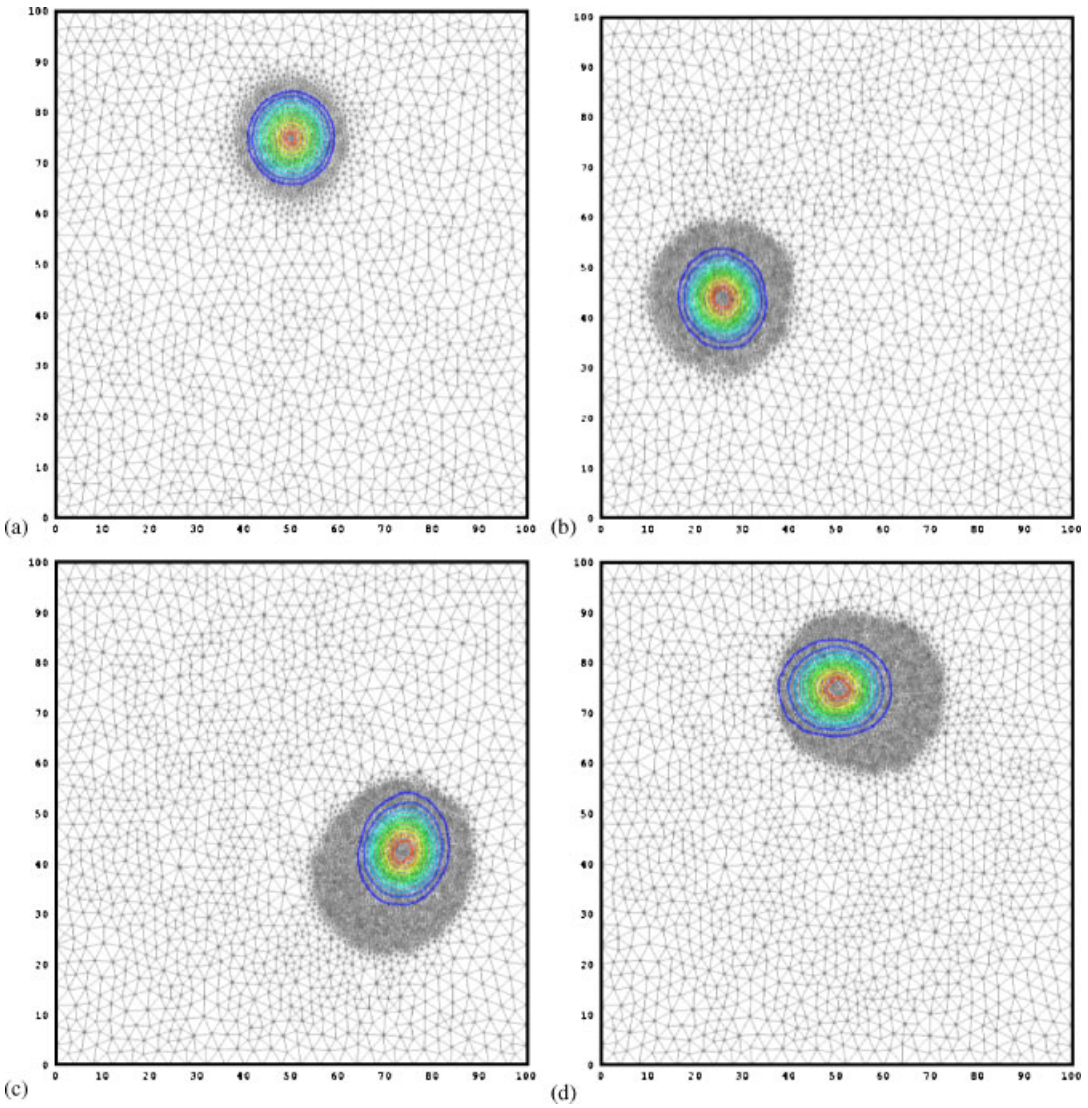

Figure 11. The initial conditions (a), and (b)–(d) the solution-adaptive grid solution at three times ending after one complete revolution.

at $(x_c, y_c) = (50, 75)$ with a maximum height of 0.975 unit and a radius of 10 units. The rotational flow field was defined in the similar manner as in the convergence study with the exception that the constant angular velocity ω, was set to 0.4. The simulation was run for 15.7079 s (time taken by the cone to complete one revolution $= 2\pi/\omega$). The unstructured mesh was defined in terms of boundary edges (100 edges on each side for the globally refined mesh and 25 edges on each side for the adaptive and coarse mesh). The adaptive mesh started with a minimum edge length of 0.337 and a maximum edge length of 4.667. As the mesh was

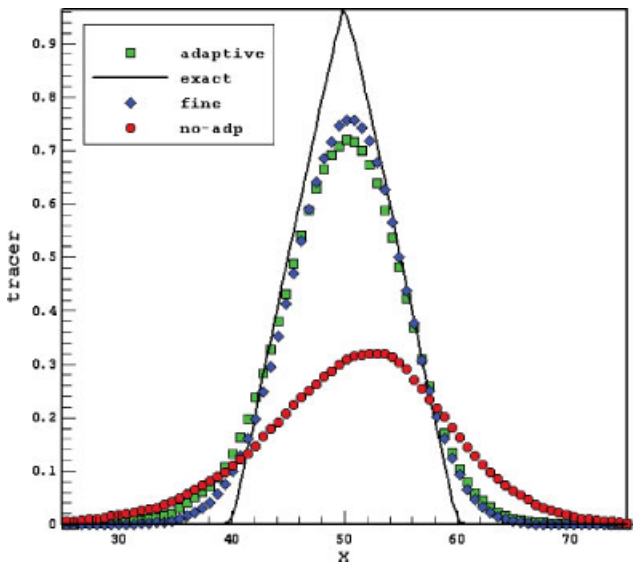

Figure 12. Comparison of a rotating cone test on the adaptive, coarse and globally refined meshes with the exact solution after one revolution. The profiles shown are at $y = 75$ for x varying from 25 to 75 ($t = 15.7079$ s).

adapted the mesh resolution varied from maximum edge length of roughly 5 and minimum edge of approximately 0.20 in different adaptation cycles. The globally fine mesh had edges ranging from 0.22 to 1.27.

The adaptation criteria was defined in terms of the cone radius. Three radii were defined—R_{cone} was set to the radius of the cone; R_{ref} was 2.5 units larger than R_{cone} and R_{coarse} was defined as 4.5 units larger than R_{cone}. The maximum and minimum allowable edge lengths were also specified. The cells were tagged for refinement if a cell with large edge lengths was found between R_{cone} and R_{ref} and cells were tagged for deletion if a cell with small edge lengths was found outside the circle defined by R_{coarse}. The refinement cycle was invoked every 15 iterations and the coarsening cycle was invoked every 150 iterations.

Figure 11 shows the tracer concentration contours at the initial time, at intermediate stages, and after one revolution for the solution-adaptive run. Figure 12 compares the concentration profiles at $y = 75$ for x between 25 and 75 with the exact solution. The adaptive run is slightly more diffusive than the globally refined mesh run (the profile for the simulation on the coarse mesh is also plotted for reference); however, overall the results are comparable and the adaptive grid solution is approximately twice as fast as the globally refined solution.

7. CONCLUSIONS

MPDATA has been implemented on an unstructured adaptive grid with excellent performance for environmental flow situations. While the scheme is not as accurate as MUSCL-type advec-

tion schemes, neither is it as computationally expensive. Apart from speed the other advantages of the MPDATA scheme are in its multidimensional nature (MUSCL-type schemes rely on Riemann solvers which are one-dimensional); and the simplicity of the method itself both in its design and implementation [25]. The efficiency in speed becomes especially crucial for real-time atmospheric flow simulations which require much CPU time for the calculations related to planetary boundary layer physics/turbulence closure, atmospheric radiation heat transfer and cloud microphysics. The benefit of implementing MPDATA on an unstructured grid comes from the flexibility that such grids provide. Static adaptation of the underlying terrain is a significant improvement in GFD over the traditional nested rectilinear grids currently used; the addition of solution-adaptive gridding provides a major (factor of 2) improvement in performance while maintaining high accuracy locally.

ACKNOWLEDGEMENTS

The development of OMEGA was begun under SAIC IR&D funding and continued with support from the Defense Threat Reduction Agency (and its predecessor agencies). In addition, the authors gratefully acknowledge Drs Doug Henn and Ian Sykes of Titan/ARAP for providing the source code for calculating the analytical solution of the deformational flow problem.

REFERENCES

1. Charney J. On the scale of atmospheric motions. *Geofysiske Publikasjoner* 1948; **17**:1–17.
2. Charney JG, Fjörtoft R, von Neumann J. Numerical integration of the barotropic vorticity equation. *Tellus* 1950; **2**:237–254.
3. Arakawa A. Computational design for long-term numerical integrations of the equations of atmospheric motion. *Journal of Computational Physics* 1966; **1**:119–143.
4. Smolarkiewicz PK. A fully multidimensional positive definite advection transport algorithm with small implicit diffusion. *Journal of Computational Physics* 1984; **54**:325–362.
5. Prusa JM, Smolarkiewicz PK. An all-scale anelastic model for geophysical flows: dynamic grid deformation. *Journal of Computational Physics* 2003; **190**:601–622.
6. Iselin J, Prusa JM, Gutowski WJ. Dynamic grid adaptation using MPDATA scheme. *Monthly Weather Review* 2002; **130**:1026–1039.
7. Hasumi H, Suginohara N. Sensitivity of a global ocean general circulation model to tracer advection schemes. *Journal of Physical Oceanography* 1999; **29**:2730–2740.
8. Baum JD, Luo H, Löhner R. Numerical simulation of a blast inside a Boeing 747. *AIAA Paper 1993-3091*, 1993.
9. Luo H, Baum JD, Löhner R, Cabello J. Implicit schemes and boundary conditions for compressible flows on unstructured meshes. *AIAA 1994-0816*, 1994.
10. Bacon DP, Ahmad N, Boybeyi Z, Dunn T, Hall MS, Lee PCS, Sarma A, Turner MD, Waight KT, Young SH, Zack JW. A dynamically adapting weather and dispersion model: the operational multiscale environment model with grid adaptivity (OMEGA). *Monthly Weather Review* 2000; **128**:2044–2076.
11. Boybeyi Z, Ahmad NN, Bacon DP, Dunn TJ, Hall MS, Lee PCS, Sarma RA, Wait TR. Evaluation of the operational multiscale environment model with grid adaptivity against the European tracer experiment. *Journal of Applied Meteorology* 2001; **40**:1541–1558.
12. Gopalakrishnan SG, Bacon DP, Ahmad NN, Boybeyi Z, Dunn TJ, Hall MS, Jin Y, Lee PCS, Mays DE, Madala RV, Sarma RA, Turner MD, Wait TR. An operational multiscale hurricane forecasting system. *Monthly Weather Review* 2002; **130**:1830–1847.
13. Baum JD, Löhner R. Numerical simulation of shock-elevated box interaction using an adaptive finite element shock capturing scheme. *AIAA Journal* 1994; **32**:682–692.
14. Schnack DD, Lottati I, Mikic Z, Satyanarayana P. A finite-volume algorithm for three-dimensional magnetodynamics on an unstructured, adaptive grid in axially symmetric geometry. *Journal of Computational Physics* 1998; **140**:71–121.
15. Girardi F, Graziani G, Klug G, Nodop K. The European tracer experiment description and summary of the ETEX project. In *ETEX Symposium on Long-range Atmospheric Transport, Model Verification and Emergency Response, Proceedings*, 13–16 May 1997, Vienna, Austria. Nodop K (ed.). EUR 7346 EN, Office for Official Publications of the European Communities: Luxembourg, 1997; 83–86.

16. Dop HV, Addis R, Fraser G, Girardi F, Graziani G, Inoue Y, Kelly N, Klug W, Kulmala A, Nodop K, Pretel J. ETEX: a European tracer experiment; observations, dispersion modeling and emergency response. *Atmospheric Environment* 1998; **32**:4089–4094.
17. Varvayanni M, Davakis E, Deligiannis P, Catsaros N. Pollutant dispersion over complex surfaces of variable landuse using unstructured prismatic grid. *Journal of Geophysical Research* 1999; **104**:275–293.
18. Ghorai S, Tomlin AS, Berzins M. Resolution of pollutant concentrations in the boundary layer using a fully 3D adaptive gridding technique. *Atmospheric Environment* 2000; **34**:2851–2863.
19. Behrens J, Dethloff K, Hiller W, Rinke A. Evolution of small-scale filaments in an adaptive advection model for idealized tracer transport. *Monthly Weather Review* 2000; **128**:2976–2982.
20. Jones RW. A nested grid for a three-dimensional model of a tropical cyclone. *Journal of the Atmospheric Sciences* 1977; **34**:1528–1553.
21. Zhang D-L, Chang H-R, Seaman NL, Warner TT, Fritsch JM. A two-way interactive nesting procedure with variable terrain resolution. *Monthly Weather Review* 1986; **114**:1330–1339.
22. Sarma A, Ahmad N, Bacon D, Boybeyi Z, Dunn T, Hall M, Lee P. Application of adaptive grid refinement to plume modeling. *Air Pollution VII*. WIT Press: Southampton, 1999; 59–68.
23. Ahmad N, Bacon D, Boybeyi S, Dunn T, Gopalakrishnan S, Hall M, Lee P, Mays D, Sarma A, Turner M, Wait T. Unstructured adaptive grid generation for geophysical flow simulations. *Numerical Grid Generation in Computational Field Simulations*, 8th International Conference held at Honolulu, Hawaii, 2002; 457–466.
24. Smolarkiewicz PK, Clark TL. The multidimensional positive definite advection transport algorithm: further development and applications. *Journal of Computational Physics* 1986; **67**:396–438.
25. Smolarkiewicz PK, Grabowski WW. The multidimensional positive definite advection transport algorithm: nonoscillatory option. *Journal of Computational Physics* 1990; **86**:355–375.
26. Godunov SK. A finite difference method for the computation of discontinous solutions of the equations of fluid dynamics. *Matematicheskii Sbornik* 1959; **47**:357–393.
27. Van Leer B. Towards the ultimate conservative difference scheme. V. A second-order sequel to Godunov's method. *Journal of Computational Physics* 1979; **32**:101–136.
28. Barth TJ, Jesperson DC. The design and application of upwind schemes on unstructured meshes. *AIAA Paper 1989-0366*, 1989.
29. Smolarkiewicz PK. The multi-dimensional Crowley advection scheme. *Monthly Weather Review* 1982; **113**: 1050–1065.
30. Doswell CA. A kinematic analysis of frontogenesis associated with a nondivergent vortex. *Journal of the Atmospheric Sciences* 1984; **41**:1242–1248.
31. Burg C, Sreenivas K, Hyams D, Mitchell B. Unstructured nonlinear free surface flow solutions: validation and verification. *AIAA Paper 2002-2977*, 2002.
32. LeVeque RJ. *Finite Volume Methods for Hyperbolic Problems*. Cambridge University Press: Cambridge, 2002.
33. Jameson A, Schmidt W, Turkel E. Numerical solution of the Euler equations by finite volume method using Runge–Kutta time stepping schemes. *AIAA Paper 1981-1259*, 1981.
34. Ahmad N, Boybeyi Z, Löhner R, Sarma A. A Godunov-type scheme for atmospheric flows on unstructured grids: scalar transport. *Pure and Applied Geophysics* 2005, in press.
35. Staniforth A, Cote J, Pudykiewicz J. Comments on "Smolarkiewicz's deformational flow". *Monthly Weather Review* 1987; **115**:894–900.
36. Sykes RI, Henn DS. Representation of velocity gradient effects in a Gaussian puff model. *Journal of Applied Meteorology* 1995; **34**:2715–2723.
37. Hólm EV. A fully two-dimensional, nonoscillatory advection scheme for momentum and scalar transport equations. *Monthly Weather Review* 1995; **123**:536–552.

